INORGANIC CHEMISTRY FRONTIERS

RESEARCH ARTICLE

View Article Online
View Journal | View Issue

Cite this: *Inorg. Chem. Front.*, 2023, **10**, 3082

Construction of a self-supported dendrite-free zinc anode for high-performance zinc–air batteries†

Chuancheng Mou,[a,c] Yujia Bai,[c] Chang Zhao,[c] Genxiang Wang,[c] Yi Ren,[a,c] Yijian Liu,[c] Xuantao Wu,[c] Hui Wang *[b,c] and Yuhan Sun*[a,b,c]

Zinc-anode-based batteries are widely used in energy storage devices due to their low cost, high-energy density, and environmental friendliness. However, the fatal dendrite growth of the zinc anode during cyclic plating and stripping processes severely affects the service life of the batteries. Herein, a ZIF-8-derived Zn-ZnO@C-550 anode, *i.e.* ZnO nanoarrays grown *in situ* on the surface of zinc foil *via* chemical deposition followed by hydrothermal synthesis and annealing, is designed for zinc–air batteries. With this prepared self-supported anode, the assembled zinc–air battery exhibits excellent discharge performance (995.77 mA h) compared to the same size of zinc foil, and remarkable cycling performance (more than 1200 cycles at a large current density of 10 mA cm^{-2}) with dendrite growth being suppressed. The superior anti-dendritic properties of the fabricated Zn-ZnO@C-550 anode can be attributed to the highly ordered array structure of the Zn anode, which allows a homogeneous zinc ion concentration to avoid the growth of metallic zinc clusters, as confirmed by a simulation of the electrode current density distribution. The reversibility of Zn^{2+} plating/stripping in this work provides a promising strategy for preparing a dendrite-free metal anode of these Zn-related batteries.

Received 15th February 2023,
Accepted 31st March 2023

DOI: 10.1039/d3qi00279a

rsc.li/frontiers-inorganic

Introduction

The rapid consumption of fossil energy is bringing about a serious crisis of energy and the environment; hence it is important to develop renewable and sustainable clean energy resources to replace fossil fuels.[1,2] Currently, lithium-ion batteries are widely used in laptops, mobile phones and electric vehicles due to their excellent cycle performance.[3] However, Li-ion batteries have many safety concerns, which severely restrict their further development. For this reason, zinc–air batteries (ZABs) are being pushed forward as alternatives due to their safe aqueous electrolyte, higher specific capacity (1086 W h kg^{-1}),[4–6] and the abundant zinc resources for zinc anodes, including metal zinc, zinc oxide and zinc composites.[7–9] Thus, ZABs with multiple advantages of low cost,[10] environmental friendliness, and high energy density have been considered to be one of the most promising battery technologies.[11] However, poor cycling stability, the existence of side reactions (anode passivation, self-corrosion of Zn and hydrogen evolution corrosion), and zinc dendrite growth severely limit the commercial development of zinc–air batteries.[12–14] One of the most common fatal problems is the growth of zinc dendrites, which will pierce the separator and lead to short-circuits in ZABs.

Owing to the fact that dendrite growth is generally induced by the nonuniform distribution of ions in the vicinity of a zinc electrode with a limited specific surface area, the formation of dendrites is inevitable.[15] The excessive local current density and unrestricted 2D diffusion of Zn^{2+} formed on a planar zinc electrode with low surface area easily lead to dendrite generation during the cycling process.[16,17] To improve the performance of a zinc anode, plenty of efforts have been made structurally to inhibit dendrite growth. The main solutions to the above problems include two aspects: (1) optimize the interface between electrode and electrolyte to enhance the uniform distribution of zinc ions. A planar zinc electrode[18] is limited by its own contact area with the electrolyte, and often forms a nonuniform passivation layer.[19] As a result, some areas with higher local concentration could induce the growth of zinc protrusions. Subsequently, crystal anisotropy and the cusp effect[20,21] accelerate dendrite growth. To ensure uniformity of electroplating, researchers have built a nano-porous coating as a buffer layer between the electrode and the electrolyte. For example, in the construction of a (0 0 1)-faceted TiO_2 layer, the relatively low zinc affinity,[22] porous nano-$CaCO_3$ coating,[23] and

[a]*School of Physical Science and Technology, ShanghaiTech University, Shanghai, 201210, China. E-mail: sunyh@sari.ac.cn*
[b]*Institute of Carbon Neutrality, ShanghaiTech University, Shanghai, 201210, China. E-mail: wanghh@sari.ac.cn*
[c]*Shanghai institute of Cleantech Innovation, Shanghai, 201616, China*
† Electronic supplementary information (ESI) available. See DOI: https://doi.org/10.1039/d3qi00279a

HfO_2 coating[14] all serve the purpose of regulating the deposition of zinc and inhibiting the growth of dendrites. (2) Construct a three-dimensional network[24] which has a larger specific surface areas with more steric sites. A three-dimensional network designed to promote certain Zn nucleation can not only mitigate dendrite formation, but also provide more vacancies for the volume expansion caused by Zn deposition, thus avoiding electrode deformation. In previous work, a three-dimensional Zn/CNT foam skeleton,[25] h-WO_3/3DG zinc anode,[26] and 3D porous Zn[19] were constructed to enlarge the contact area between electrode and electrolyte. Moreover, a three-dimensional structure can also improve the wettability of the electrode surface, thus increasing mass transport, and theoretically improving reversibility by confining the plating/stripping process within the structure.[25,27]

In this work, self-supported zinc anodes with highly ordered ZnO nanoarrays grown *in situ* on the surface of zinc foil were constructed for zinc–air batteries. The Zn plating/stripping process is restricted in the arrays, thus achieving dendrite-free growth in a macro sense. In addition, the highly ordered nanoarray structure increases the wettability of the electrode and improves charge transfer efficiency at the same time. Through this research, it was found that the Zn-ZnO@C-550 electrode had a lower polarization and a prolonged lifespan of over 1200 cycles, which provides a promising idea for dendrite-free zinc anodes of zinc–air batteries.

Results and discussion

Fig. 1a shows a schematic diagram of the fabrication of a Zn-ZnO@C-550 composite electrode. Firstly, highly ordered ZnO arrays were formed on the surface of zinc foil (Zn–ZnO) by chemical deposition. And then, a layer of ZIF-8 was grown *in situ* on the ZnO-nanoarray-coated zinc foil (Zn-ZnO@ZIF-8) *via* a hydrothermal reaction. Finally, the ZIF-8 layer evolved into N-doped carbon, undergoing annealing at 550 °C in an Ar atmosphere. Zn-ZnO@ZIF-8 precursors treated at other temperatures (500 °C and 600 °C) were prepared as control samples.

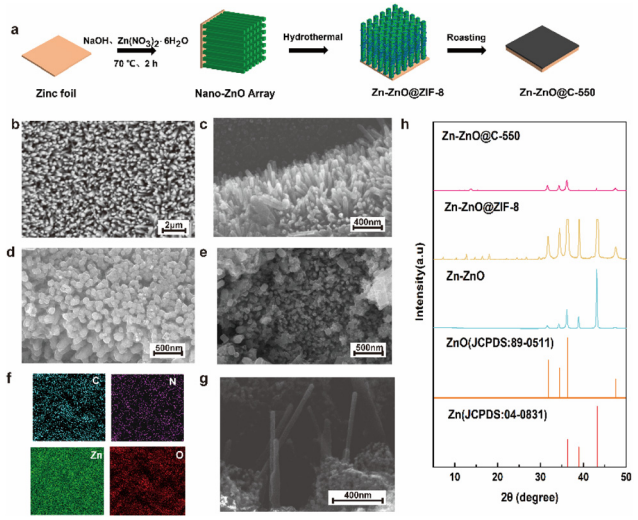

Fig. 1 (a) Schematic diagram of the synthesis process of the Zn-ZnO@C-550 electrode. SEM images of (b) nano-ZnO array, (c) cross-sectional image of nano-ZnO array, (d) Zn-ZnO@ZIF-8 and (e) Zn-ZnO@C-550, and (f) EDX elemental mappings of Zn-ZnO@C-550, (g) cross-sectional image of Zn-ZnO@C-550. (h) XRD patterns of nano-ZnO array, Zn-ZnO@ZIF-8 and Zn-ZnO@C-550, respectively.

The morphologies were then revealed by SEM. The SEM image of zinc foil shows its rather smooth surface (Fig. S1a, in ESI†). After treatment by chemical deposition, a highly uniform and ordered rod-like ZnO nanoarray structure is formed on the surface (Fig. 1b and c). The density of the array can be controlled by the concentration of NaOH (Fig. S1d and e†). After the secondary growth of ZIF-8 on the surface of Zn–ZnO, a uniform layer coating on the ZnO nanoarray is observed on the surface (Fig. 1d), which to certain extent preserves the high order of the array structure. After further calcination treatment of Zn-ZnO@ZIF-8, rough rod-shaped ZnO coated with an N-doped carbon layer are exposed on the electrode surface (Fig. 1e and g). The EDX elemental mapping analysis indicates that C, N, O and Zn are uniformly distributed in the Zn-ZnO@C-550 electrode (Fig. 1f).

The XRD technique was used to reveal the crystal phase of these prepared samples. XRD patterns of both Zn-ZnO@ZIF-8 and Zn-ZnO@C-550 show characteristic peaks of ZnO and Zn. The characteristic peaks located at 31.840°, 34.502°, 36.332°, and 47.652° correspond to (1 0 0), (0 0 2), (1 0 1), and (1 0 2) crystal planes, respectively. While peaks at 36.289°, 38.993° and 43.220° correspond to (0 0 2), (1 0 0), and (1 0 1) crystal planes of Zn metal, respectively (Fig. 1h). The control samples treated at 500 °C and 600 °C show similar XRD patterns to those of Zn-ZnO@C-550 (Fig. S2, ESI†). Remarkably, the disappearance of some of the peaks attributed to ZIF-8 in these calcined electrodes indicates that carbonization of ZIF-8 has occurred.[28]

To further understand the principle of zinc deposition on the zinc foil and Zn-ZnO@C-550 surface, the current distribution on the electrodes in electrolyte was simulated using Fluent. The calculation shows that the current density tends to accumulate on zinc protrusions, as shown in Fig. 2a, where the maximum current density appears at the tip. This further proves how zinc protrusion exacerbate dendrite formation. From a macro perspective, as the reaction goes on, the uneven deposition causes a rough and uneven electrode surface, which in turn affects the charge distribution on the electrode surface. As shown in Fig. 2a, the charge accumulation at the tip attracts more Zn^{2+}, which intensifies the inhomogeneous deposition on the bump and leads to the growth of Zn dendrites (Fig. 2c). They eventually form dead zinc deposits on the bottom of the battery as the reaction continues, reducing the battery life. In contrast, the calculation shows that the current density is higher on the sides of the arrays, where zinc deposits are concentrated around them, as shown in Fig. 2b. At the same time, the array structure can regulate the deposition behavior of zinc and confine it to the interior of the void. This structure is more attractive to zinc ions and promotes the uniform deposition of zinc.

To investigate the role of the constructed structure of the Zn-ZnO@C-550 electrode in the suppression of dendrite

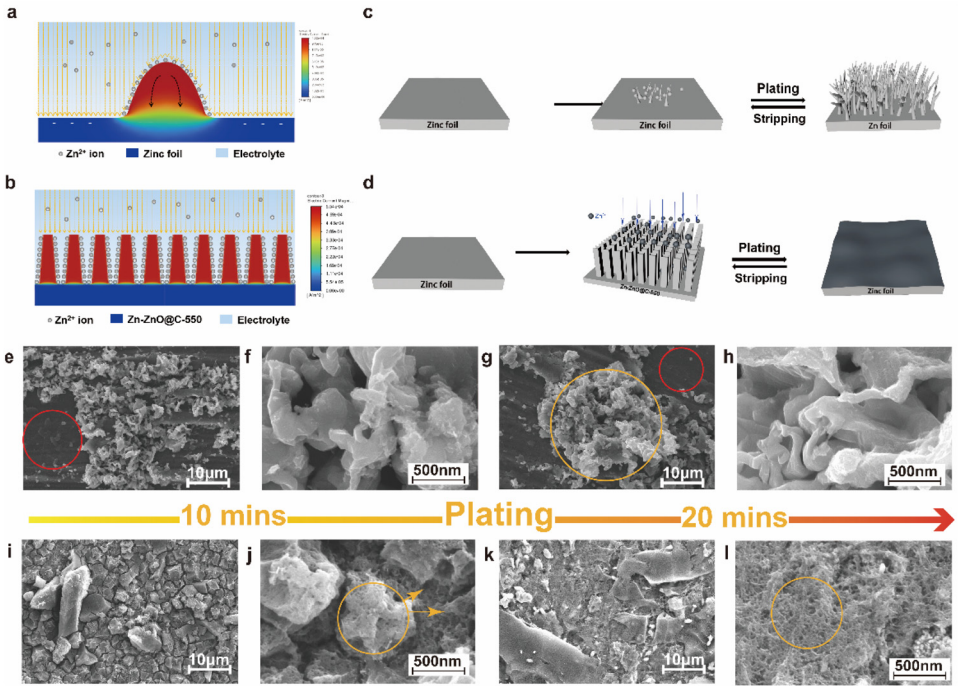

Fig. 2 Simulations of the relative intensity distributions of localized current density for (a) zinc foil and (b) Zn-ZnO@C-550. (c and d) Schematics of bare zinc foil and Zn-ZnO@C-550 during repeated plating/stripping behavior. Morphological evolution of (e–h) pristine Zn and (i–l) Zn-ZnO@C-550 electrodes during the plating process at a current density of 5.0 mA cm^{-2} with different durations.

growth, the process of morphological evolution during repeated plating experiments was recorded by the SEM technique. The plating experiments are shown in Fig. S4.† As shown in Fig. 2e and g, no metallic Zn deposits were found in the red circles; this indicates that the reaction rate is slow here. The uneven charge distribution on the electrode surface may lead to different reaction rates on its surface, which will ultimately affect the ion concentration distribution on the electrode surface. During cycling, some small zinc particles initially deposit on the surface of the zinc foil with a relatively balanced electric field.[29] Subsequently, charges accumulate at the tips of these small zinc deposits, which serve as a charge center for further zinc deposition.[30,31] The initial sedimentary nucleation shows a strong electric field effect, which could exacerbate dendrite growth.[27,32] Due to a memory effect, dendrite growth at this position will intensify. As shown in Fig. 2g, a large number of metallic Zn clusters appeared in the orange circles, which further confirmed that the tip effect accelerates the deposition of metallic zinc. When it grows to a certain length, the dendrite could cause short-circuit failure. As expected, the SEM images of the morphological evolution of zinc foil after undergoing Zn^{2+} deposition behavior in alkaline electrolytes reveal that the surface of the zinc foil is composed of random zinc particles, which gradually accumulate to form large zinc cluster protrusions with deposition from 10 to 20 min (Fig. 2e–h). The non-uniform deposition on zinc foil can be attributed to the limited ion and electron transmission path caused by its small specific surface area, poor wettability, and increased resistance induced by a ZnO passivated layer, which will greatly degrade its reversibility for a zinc–air battery.[19] By contrast, the Zn-ZnO@C-550 electrode presents an entirely different deposition process (Fig. 2i–l). The deposition process on the surface of the Zn-ZnO@C-550 electrode starts from the nucleation and deposition of different crystal planes on the bottom surface, and then extends and grows to the surrounding voids (Fig. 2j, shown in orange circles). After 20 minutes, it is filled to form a flat and dendrite-free zinc surface (Fig. 2l, shown in orange circles). Then the electrochemically active surface areas (ECSAs) of Zn-ZnO@C-550 and Zn foil are evaluated by double-layer capacitance (C_{dl}). Zn-ZnO@C-550 possesses a larger C_{dl} [33] than Zn foil, indicating its large surface area (Fig. S5, ESI†). Therefore, the 3D structure of the Zn-ZnO@C-550 electrode possesses a large surface area with numerous voids, and can provide enough space for the volume expansion of the zinc electrode during deposition,[19] which eventually prevents battery decay.

The electrochemical stability of bare zinc foil and the Zn-ZnO@C-550 composite electrode was inspected by assembling them into a full zinc–air battery with 4 M aqueous KOH as electrolyte, an air electrode as the cathode and zinc foil as the anode. In the discharging process (Fig. 3a), the voltage of zinc foil decays fast, which may be attributed to the uneven current distribution on the electrode surface. As shown in Fig. 3b, LSV results show that with increasing current density, the overpotential of bare zinc foil increases, and the overall battery performance deteriorates dramatically. This may be attributed to the self-discharge reaction on the surface of bare zinc foil,[34] which accelerates the corrosion process and leads to voltage

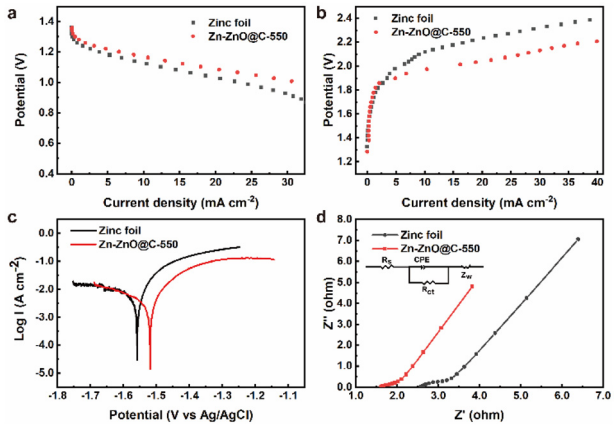

Fig. 3 (a and b) Comparison of the discharge/charge polarization curves of zinc foil and Zn-ZnO@C-550 in a zinc–air battery, respectively. (c) Linear polarization curves of zinc anodes measured with a scanning speed of 0.17 mV s^{-1} relative to the open circuit voltage in the voltage range of −0.2 V to 0.4 V (*vs.* Ag/AgCl). (d) Impedance test of bare zinc foil and the Zn-ZnO@C-550 composite electrode.

instability. It is worth noting that the cell with Zn-ZnO@C-*X* as anode shows a certain improvement in discharge performance (Fig. S6a, ESI†). A comparison of charge and discharge performance shows that the overall performance of the Zn-ZnO@C-550 battery is superior to that of Zn foil. During the discharge process (Fig. 3a), the Zn-ZnO@C-550 battery exhibits higher voltage at the same current density, indicating its superior corrosion resistance and robust stability under high current density. In the charging process (Fig. 3b), the Zn-ZnO@C-550 battery exhibits lower overpotential, which could reflect the relatively lower cell resistance and better zinc deposition performance. The improved cell performance may be attributed to the array structure of the Zn-ZnO@C-550 surface which is conducive to the homogeneous dispersion of the local Zn^{2+} concentration, to achieve the purpose of uniform deposition and suppression of dendrite growth (Fig. 2i–l).

To evaluate the corrosion resistance of pristine zinc foil and Zn-ZnO@C-550, the electrochemical performance of the anodes was examined with a three-electrode setup. Fig. 3c shows the corrosion resistance profiles of pristine zinc foil and Zn-ZnO@C-550. It illustrates the linear polarization curves[35] of the two kinds of electrode, which can be used to calculate E_{corr} and j_{corr}.[36] Notably, the current fluctuations in Fig. 3c may possibly be caused by the corrosion passivation of zinc and the hydrogen evolution reaction in corrosive liquids.[37,38] The data in Table 1 was obtained by fitting the data to observe the corrosion of the metal anode and cathode. The corrosion inhibition efficiency is calculated with the following formula (eqn (1)):[39]

$$\text{j.E}\% = \frac{({j_{corr}}^0 - j_{corr})}{{j_{corr}}^0} \times 100\% \quad (1)$$

where ${j_{corr}}^0$ and j_{corr} represent the corrosion current densities of pristine zinc foil and Zn-ZnO@C-*X* (*X* = 500, 550, 600), respectively. A lower corrosion current density indicates better corrosion resistance.[40] As shown in Table 1, the Zn-ZnO@C-550 composite electrode has a lower current density. The corrosion polarization curve of the original zinc foil is 11.50 mA cm^{-2}. In contrast, the self-corrosion potential of Zn-ZnO@C-*X* moved in a positive direction as the zinc anodic reaction decreased (Fig. S7, ESI†). With original zinc foil as blank samples, the corrosion inhibition rates of the Zn-ZnO@C-500, Zn-ZnO@C-550 and Zn-ZnO@C-600 electrodes were calculated to be 40.16%, 56.83% and 41.77%, respectively (Table 1). The corrosion current of the Zn-ZnO@C-550 electrode reached 4.96 mA cm^{-2}. The results indicate that the carbon coating on Zn plays a key role in protecting Zn from corrosion in KOH electrolyte[41] by reducing the direct contact between zinc and the electrolyte, and enhancing the hydrogen evolution overpotential. It can be seen from Fig. S8, ESI† that the zinc foil electrode was subjected to corrosion fracture when immersed in KOH for 150 h. The Zn-ZnO@C-550 electrode had good integrity, which further confirmed the corrosion resistance of the Zn-ZnO@C-550 electrode.

Table 1 Parameters for the corrosion of bare zinc foil and Zn-ZnO@C-*X* modified Zn electrodes

Sample	E_{corr} (V *vs.* Ag/AgCl)	j_{corr} (mA cm^{-2})	j.E (%)
Zinc foil	−1.62	11.50	N/A
Zn-ZnO@C-500	−1.55	6.88	40.16
Zn-ZnO@C-550	−1.56	4.96	56.83
Zn-ZnO@C-600	−1.54	6.70	41.77

Fig. 3d and S9, ESI† display the EIS performance of bare zinc foil and Zn-ZnO@C-*X*, respectively. The EIS curves were analyzed using ZView software based on an equivalent circuit (inset Fig. 3d) and the best fitting results are listed in Table S2, ESI.† As can be seen from the impedance diagram, it consists mainly of a semicircle in the high-frequency field and a sloping straight line in the low-frequency field. The high-frequency region is mainly controlled by the electrode reaction kinetics. The lower resistance of the Zn-ZnO@C-550 electrode is mainly attributed to the fact that this electrode has a larger contact area with the electrolyte and better electrode wettability, which facilitates the charge transfer process and thus possesses a smaller charge transfer resistance (R_{ct}) than the other control electrodes. The low-frequency region is mainly controlled by the diffusion process of the reaction products. For zinc foil, however, a large amount of ZnO formed on foil leads to the rough surface of the zinc foil after corrosion, severely limiting the zincate diffusion process, thus producing a rather high EIS impedance in zinc foil. To further investigate the influence of temperature on the reaction kinetic performance of Zn-ZnO@C-550, the EIS impedance of the electrode at different temperatures was tested. Based on the classical Arrhenius law, the EIS impedance plots at different temperatures were fitted, as shown in Fig. S10, ESI,† which shows that the dissolution energy base of the Zn-ZnO@C-550 cell is 21.3 kJ mol^{-1}, smaller than that of a Zn foil cell (49.2 kJ mol^{-1}). The smaller activation energy barrier for Zn-

ZnO@C-550 demonstrates the better Zn^{2+} dissolution ability on its surface,[42,43] which may be attributed to more vacancies on the Zn-ZnO@C-550 surface promoting the rapid diffusion of Zn^{2+}, thus significantly lowering the energy barrier.[44] Moreover, to reveal the electrical and ionic conductivity of the prepared electrodes, their conductivities were calculated according to eqn (1), ESI.† The conductivities of zinc foil, Zn-ZnO and Zn-ZnO@C-550 electrode were 401.7, 263.7 and 640.3 ms cm^{-1}, respectively (Table S2, ESI†). In contrast, the conductivity of the ZnO array electrodes was relatively poor. This indicates that the ZIF-8-derived carbon material has reasonable electrical conductivity.[45]

At the same time, a side reaction such as passivation will occur in the discharge process, which will increase the consumption of zinc foil and reduce the lifespan of the zinc. The Zn-ZnO@C-550 composite reduces the direct contact between zinc foil and electrolyte, and inhibits side reactions to some extent. As a preliminary test of Zn and Zn-ZnO@C-*X* performance, four zinc electrodes with the same quality and specifications were assembled and discharged to 0.8 V with a current density of 10 mA cm^{-2} at ambient temperature (Fig. 4a and S11, ESI†).[46–48] Remarkably, the curve of the Zn-ZnO@C-550 electrode shows a short drop followed by a rise at the initial stage of the discharge. The voltage decay comes mainly from the ohmic polarization at the start of discharge, where the load current produces a certain voltage drop across the internal resistance of the cell.[49] Then, as the electrolyte penetrates further into the voids of the electrode surface, the voltage loss will reduce as the ohmic polarization decreases, and the voltage will rise back up until it is stable.[50] As shown in Table S3,† the capacity of a battery with Zn-ZnO@C-550 as anode is 995.77 mA h, 2.5 times more than that of bare zinc foil of the same size (387.63 mA h). The uniform discharge of the Zn-ZnO@C-550 electrode is attributed to the higher utilization of zinc. As shown in Fig. 4b, the potential of the oxidation current peak in the anodic polarization curve of the Zn-ZnO@C-550 electrode shifts to higher potential compared with zinc foil, indicating that the passivation of the zinc electrode was delayed due to the protection of the carbon layer. That is, the oxidation of Zn is hindered by the carbon layer to some degree.

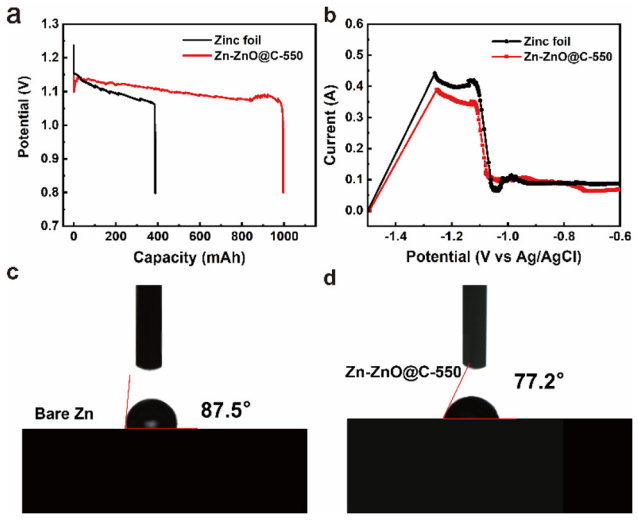

Fig. 4 (a) Discharge performance curve of a zinc–air battery with zinc foil or Zn-ZnO@C-550 as anode at a current density of 10 mA cm^{-2}. (b) Anodic polarization curve in a three-electrode configuration. (c and d) Wetting angle tests for zinc and Zn-ZnO@C-550.

The Zn-ZnO@C-550 electrode also exhibits high rate stability performance that keeps working within the wide current density range of 1.0 mA cm^{-2} to 10.0 mA cm^{-2}, as shown in Fig. 5b. The long-term cycling performances of the zinc–air batteries were investigated at a charge/discharge current density of 10 mA cm^{-2}. Fig. 5c shows that the charge–discharge of the Zn-ZnO@C-550 composite electrode has stable plateaus and the voltage attenuation process is much lower than that of a bare zinc foil electrode. After 100 cycles, the overpotential of the zinc foil battery starts to increase. This may be due to the increased dendrite growth on the electrode surface (Fig. 5h); the migration of $Zn(OH)_4^{2-}$ (Fig. 5a) on the electrode surface is hindered, and the formation of ZnO on the electrode surface finally affects the progress of the reaction. In contrast, the Zn-ZnO@C-550 battery can be cycled stably for more than 1200 cycles without significant voltage fluctuation. This is mainly attributed to the carbon coating for electrode protection. The Zn-ZnO@C-500/600 cycle performances are shown in Fig. S12, ESI.† This structure makes the current distribution on the zinc electrode more consistent, thus suppressing the growth of dendrites and enhancing battery life.[51] In addition, the cycle life of a cell with a ZIF-8 electrode (Zn@C-550) was tested, which can be maintained only over 400 cycles, far inferior to that of the Zn-ZnO@C-550 cell (1200 cycles) (Fig. S13†). Therefore, the array structure plays an important role in advancing the durability of the electrode. As shown in Fig. 5d, in the initial charging process, the overpotential of the bare zinc electrode is 912.9 mV, which is much higher than that of the Zn-ZnO@C-550 composite electrode (624.3 mV). The higher overpotential of the bare zinc electrode may be attributed to the passivation reaction that requires more energy to activate. In other words, the combined use of N doping and carbon coating can effectively restrain electrochemical polarization, especially at high current density. At the 45th and 75th cycles, the overpotential of the battery with zinc foil decreases, but remains at more than 700 mV (Fig. 5e and f). The Zn-ZnO@C-550 battery is stable, and the overpotentials of the 1st, 45th, and 75th cycles are all maintained at about 600 mV. EIS measurements verify that the interfacial transfer resistance R_{ct} of the Zn-ZnO@C-550 composite electrode is only 0.0549 Ω. An optical contact angle measuring instrument (KJ-625) was used to measure the contact angles of bare zinc foil and Zn-ZnO@C-550, respectively. As shown in Fig. 4c and d, the wetting angle of bare zinc foil is 87.5°, and that of the Zn-ZnO@C-550 composite electrode is 77.2°. Better contact between electrode and electrolyte improves ion transfer efficiency between the KOH-based electrolyte and the zinc electrode.[52] Electrochemical measurements verify that Zn-ZnO@C-550 plays an important role in improving battery performance and inhibiting dendrite growth.

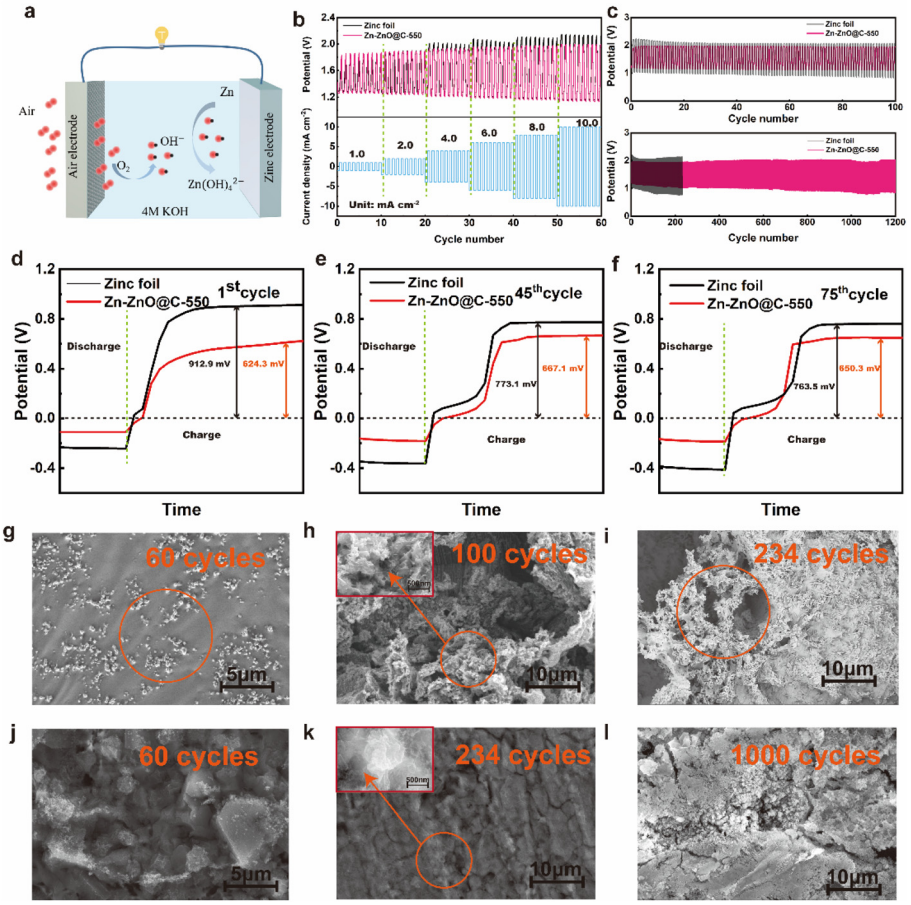

Fig. 5 (a) Schematic illustration of the operation of a zinc–air battery. (b) Rate performance of zinc foil and the Zn-ZnO@C-550 composite electrode at current densities from 1.0 to 10.0 mA cm^{-2}. (c) Cyclic voltammetry curves of bare zinc foil and the Zn-ZnO@C-550 composite electrode in the first 100 cycles. CV curve of bare zinc foil and the Zn-ZnO@C-550 composite electrode at a current density of 10 mA cm^{-2}. (d) Comparison of overpotential performance between bare zinc foil and the Zn-ZnO@C-550 composite electrode in the first charging process. (e and f) Diagram of overpotential performance changes of bare zinc foil and Zn-ZnO@C-550 during the 45th and 75th cycles. (g–i) SEM of the zinc foil when zinc foil is used as an anode in a zinc–air battery after 60, 100, 234 cycles, respectively. (j–l) SEM of the Zn plate when Zn-ZnO@C-550 is used as an anode in a zinc–air battery after 60, 234, 1000 cycles, respectively.

To demonstrate the role of our well-crafted anode in suppressing dendrite growth, scanning electron microscopy (SEM) of the zinc foil anode or the Zn-ZnO@C-550 anode after cycling were investigated. After 60 cycles, the initially smooth surface of zinc foil (Fig. S1a, ESI†) transforms into a rough surface with a large number of agglomerated Zn protrusions (Fig. 5g, shown in the orange circle). Consequently, initial Zn nucleation sites evolve into protuberances (as shown in Fig. 2g), where zinc ions tend to migrate to the tip site, inducing deposition of dendritic structures.[24,53] Under 100 cycle life, it can be seen from the electron microscope image that a large number of holes are corroded on the surface of the electrode and a large number of flaky zinc dendrites grow (Fig. 5h, shown in the orange circle and Fig. S14g†). With the continuous progress of the reaction, the dendrites on the electrode surface continued to intensify, and a large amount of white ZnO was formed on the surface, as shown in Fig. 5i (orange circle) and Fig. S14h, ESI.† By contrast, the Zn-ZnO@C-550 electrode illustrates an entirely different deposition process. The metallic zinc is deposited around different planes of the crystal, avoiding the agglomeration of metallic zinc during deposition, as shown in Fig. 5j. As the number of cycles increases, with more zinc deposited on the surface, a uniform surface eventually forms on the electrode, as shown in Fig. 5k. At 400 and 500 cycles, as the surface zinc thickens, no obvious flaky zinc formation is seen (Fig. S14b–e, ESI†). After 1000 cycles, metal zinc was uniformly deposited on the surface of the electrode, and no obvious lamellar dendrites were found, as shown in Fig. 5l and S14f, ESI.† The formation of irregular zinc was reduced and dendrite growth was inhibited. This is exactly how the protection of the carbon coating inhibits the side reactions on the electrode surface, thus achieving a higher utilization efficiency of the electrode.[54,55] Thus, the difference in the morphological evolution between pristine zinc and the Zn-ZnO@C-550 electrode during the plating/stripping process confirms the spatially confined Zn growth and the superior Zn dendrite suppression in the Zn-ZnO@C-550 electrode.[19]

In addition, the array structure also promotes the uniform deposition of Zn^{2+} and eventually achieves dendrite-free zinc growth. The highly ordered array structure provides enough active sites for the deposition of zinc ions, and provides enough space for the volume expansion from zinc deposition at the same time. Thus, the dendrite growth was inhibited and the battery life was improved.

Conclusion

In summary, we report Zn-ZnO@C-550 as a novel zinc anode for ZABs. The regular surface structure and high specific surface area endow the Zn-ZnO@C-550 anode with fast reaction kinetics and structural durability. Our results confirm that the ZIF-8-derived Zn-ZnO@C-550 electrode induces bottom-top Zn deposition behavior with low overpotential during plating/stripping. More importantly, the Zn-ZnO@C-550 electrode inhibits the growth of dendrite morphology. Calculations show that the uniform current density distribution on the array surface confines the zinc deposition behavior to the voids between the arrays, which is the main reason for achieving suppression of dendrite growth. It demonstrates a high discharge capacity (995.77 mA h) compared to the same size of zinc foil and excellent cycling durability of 1200 cycles at a current density of 10 mA cm^{-2}. The electrode plating/stripping with the array structure has better reversibility and shows a huge advantage in reducing the growth of dendrites, which was confirmed by simulation of the electrode current density distribution. This work provides an idea for the study of dendrite-free zinc anodes in zinc–air batteries.

Author contributions

Chuancheng Mou conducted most of the experiment work under the supervision of Yujia Bai and Chang Zhao. Chuancheng Mou drafted the manuscript, which was improved by Yujia Bai and Genxiang Wang. Yuhan Sun and Hui Wang led the research. Xuantao Wu, Chuancheng Mou simulated the current distribution on the electrode surface. Yi Ren and Yijian Liu were helping Chuancheng Mou in instrumentation. The manuscript was written through contributions of all authors. All authors have given approval to the final version of the manuscript.

Conflicts of interest

There are no conflicts to declare.

Acknowledgements

This research is financially supported by the National Key Research and Development Program of China (2022YFA1504800, 2022YFA1504702 and 2022YFB4101900), the National Natural Science Foundation of China (22108289, 22279158 and 21905291), CNOOC Institute of Chemicals & Advanced Materials (YJSCZX07956YJ) and Shanghai Institute of Cleantech Innovation (E244831E01).

References

1 S. Chu and A. Majumdar, Opportunities and challenges for a sustainable energy future, *Nature*, 2012, **488**, 294–303.
2 S. Wang, S. Jiao, D. Tian, H. S. Chen, H. Jiao, J. Tu, Y. Liu and D. N. Fang, A novel ultrafast rechargeable multi–ions battery, *Adv. Mater.*, 2017, **29**, 1606349.
3 B. Dunn, H. Kamath and J.-M. Tarascon, Electrical energy storage for the grid: a battery of choices, *Science*, 2011, **334**, 928–935.
4 P. Liu, X. Ling, C. Zhong, Y. Deng, X. Han and W. Hu, Porous zinc anode design for zn-air chemistry, *Front. Chem.*, 2019, **7**, 656.
5 P. Tan, B. Chen, H. Xu, H. Zhang, W. Cai, M. Ni, M. Liu and Z. Shao, Flexible Zn–and Li–air batteries: recent advances, challenges, and future perspectives, *Energy Environ. Sci.*, 2017, **10**, 2056–2080.
6 M. Wu, G. Zhang, M. Wu, J. Prakash and S. Sun, Rational design of multifunctional air electrodes for rechargeable Zn–Air batteries: Recent progress and future perspectives, *Energy Storage Mater.*, 2019, **21**, 253–286.
7 M. Geng and D. Northwood, Development of advanced rechargeable Ni/MH and Ni/Zn batteries, *Int. J. Hydrogen Energy*, 2003, **28**, 633–636.
8 J. McBreen and E. Gannon, The electrochemistry of metal oxide additives in pasted zinc electrodes, *Electrochim. Acta*, 1981, **26**, 1439–1446.
9 H. Huang, L. Zhang, W. Zhang, Y. Gan and H. Shao, Preparation and electrochemical properties of ZnO/conductive-ceramic nanocomposite as anode material for Ni/Zn rechargeable battery, *J. Power Sources*, 2008, **184**, 663–667.
10 J. W. Choi and D. Aurbach, Promise and reality of post-lithium-ion batteries with high energy densities, *Nat. Rev. Mater.*, 2016, **1**, 1–16.
11 S.-M. Lee, Y.-J. Kim, S.-W. Eom, N.-S. Choi, K.-W. Kim and S.-B. Cho, Improvement in self-discharge of Zn anode by applying surface modification for Zn–air batteries with high energy density, *J. Power Sources*, 2013, **227**, 177–184.
12 J. Fu, R. Liang, G. Liu, A. Yu, Z. Bai, L. Yang and Z. Chen, Recent progress in electrically rechargeable zinc–air batteries, *Adv. Mater.*, 2019, **31**, 1805230.
13 J. Yu, F. Chen, Q. Tang, T. T. Gebremariam, J. Wang, X. Gong and X. Wang, Ag-modified Cu foams as three-dimensional anodes for rechargeable zinc–air batteries, *ACS Appl. Nano Mater.*, 2019, **2**, 2679–2688.
14 B. Li, J. Xue, C. Han, N. Liu, K. Ma, R. Zhang, X. Wu, L. Dai, L. Wang and Z. He, A hafnium oxide-coated dendrite-free zinc anode for rechargeable aqueous zinc-ion batteries, *J. Colloid Interface Sci.*, 2021, **599**, 467–475.

15 P. Chen, X. Yuan, Y. Xia, Y. Zhang, L. Fu, L. Liu, N. Yu, Q. Huang, B. Wang and X. Hu, An artificial polyacrylonitrile coating layer confining zinc dendrite growth for highly reversible aqueous zinc–based batteries, *Adv. Sci.*, 2021, **8**, 2100309.
16 M. Li, J. Meng, Q. Li, M. Huang, X. Liu, K. A. Owusu, Z. Liu and L. Mai, Finely Crafted 3D Electrodes for Dendrite–Free and High–Performance Flexible Fiber–Shaped Zn–Co Batteries, *Adv. Funct. Mater.*, 2018, **28**, 1802016.
17 G. Zhang, X. Zhang, H. Liu, J. Li, Y. Chen and H. Duan, 3D–Printed Multi–Channel Metal Lattices Enabling Localized Electric–Field Redistribution for Dendrite–Free Aqueous Zn Ion Batteries, *Adv. Energy Mater.*, 2021, **11**, 2003927.
18 J. Zheng, T. Tang, Q. Zhao, X. Liu, Y. Deng and L. A. Archer, Physical orphaning versus chemical instability: Is dendritic electrodeposition of Li fatal?, *ACS Energy Lett.*, 2019, **4**, 1349–1355.
19 W. Wang, G. Huang, Y. Wang, Z. Cao, L. Cavallo, M. N. Hedhili and H. N. Alshareef, Organic Acid Etching Strategy for Dendrite Suppression in Aqueous Zinc–Ion Batteries, *Adv. Energy Mater.*, 2022, 2102797.
20 F. Shi, A. Pei, A. Vailionis, J. Xie, B. Liu, J. Zhao, Y. Gong and Y. Cui, Strong texturing of lithium metal in batteries, *Proc. Natl. Acad. Sci. U. S. A.*, 2017, **114**, 12138–12143.
21 K. Wang, P. Pei, Z. Ma, H. Chen, H. Xu, D. Chen and X. Wang, Dendrite growth in the recharging process of zinc–air batteries, *J. Mater. Chem. A*, 2015, **3**, 22648–22655.
22 Q. Zhang, J. Luan, X. Huang, Q. Wang, D. Sun, Y. Tang, X. Ji and H. Wang, Revealing the role of crystal orientation of protective layers for stable zinc anode, *Nat. Commun.*, 2020, **11**, 1–7.
23 L. Kang, M. Cui, F. Jiang, Y. Gao, H. Luo, J. Liu, W. Liang and C. Zhi, Nanoporous $CaCO_3$ coatings enabled uniform Zn stripping/plating for long–life zinc rechargeable aqueous batteries, *Adv. Energy Mater.*, 2018, **8**, 1801090.
24 W. Lu, C. Xie, H. Zhang and X. Li, Inhibition of zinc dendrite growth in zinc–based batteries, *ChemSusChem*, 2018, **11**, 3996–4006.
25 Y. Zhou, X. Wang, X. Shen, Y. Shi, C. Zhu, S. Zeng, H. Xu, P. Cao, Y. Wang and J. Di, 3D confined zinc plating/stripping with high discharge depth and excellent high-rate reversibility, *J. Mater. Chem. A*, 2020, **8**, 11719–11727.
26 X. Chen, R. Huang, M. Ding, H. He, F. Wang and S. Yin, Hexagonal WO3/3D Porous Graphene as a Novel Zinc Intercalation Anode for Aqueous Zinc-Ion Batteries, *ACS Appl. Mater. Interfaces*, 2022, **14**(3), 3961–3969.
27 W. Guo, Z. Cong, Z. Guo, C. Chang, X. Liang, Y. Liu, W. Hu and X. Pu, Dendrite-free Zn anode with dual channel 3D porous frameworks for rechargeable Zn batteries, *Energy Storage Mater.*, 2020, **30**, 104–112.
28 R. Yuksel, O. Buyukcakir, W. K. Seong and R. S. Ruoff, Metal–organic framework integrated anodes for aqueous zinc–ion batteries, *Adv. Energy Mater.*, 2020, **10**, 1904215.
29 Q. Zhang, J. Luan, L. Fu, S. Wu, Y. Tang, X. Ji and H. Wang, The three–dimensional dendrite–free zinc anode on a copper mesh with a zinc–oriented polyacrylamide electrolyte additive, *Angew. Chem.*, 2019, **131**, 15988–15994.
30 Q. Li, S. Zhu and Y. Lu, 3D porous Cu current collector/Li–metal composite anode for stable lithium–metal batteries, *Adv. Funct. Mater.*, 2017, **27**, 1606422.
31 X. B. Cheng, T. Z. Hou, R. Zhang, H. J. Peng, C. Z. Zhao, J. Q. Huang and Q. Zhang, Dendrite–free lithium deposition induced by uniformly distributed lithium ions for efficient lithium metal batteries, *Adv. Mater.*, 2016, **28**, 2888–2895.
32 M. Liu, X. Pu, Z. Cong, Z. Liu, T. Liu, Y. Chen, J. Fu, W. Hu and Z. L. Wang, Resist-dyed textile alkaline Zn microbatteries with significantly suppressed zn dendrite growth, *ACS Appl. Mater. Interfaces*, 2019, **11**, 5095–5106.
33 Y. Wang, Y. Zhao, L. Liu, W. Qin, S. Liu, J. Tu, Y. Qin, J. Liu, H. Wu and D. Zhang, Mesoporous single crystals with Fe–rich skin for ultralow overpotential in oxygen evolution catalysis, *Adv. Mater.*, 2022, **34**, 2200088.
34 T.-H. Wu, Y. Zhang, Z. D. Althouse and N. Liu, Nanoscale design of zinc anodes for high-energy aqueous rechargeable batteries, *Mater. Today Nano*, 2019, **6**, 100032.
35 Z. Wang, L. Dong, W. Huang, H. Jia, Q. Zhao, Y. Wang, B. Fei and F. Pan, Simultaneously regulating uniform Zn2+ flux and electron conduction by MOF/rGO interlayers for high-performance Zn anodes, *Nano-Micro Lett.*, 2021, **13**, 1–11.
36 X. Fan, Z. Yang, W. Long, B. Yang, J. Jing and R. Wang, The preparation and electrochemical performances of the composite materials of CeO_2 and ZnO as anode material for Ni–Zn secondary batteries, *Electrochim. Acta*, 2013, **108**, 741–748.
37 L. Q. Gong, H. G. Fu and X. H. Zhi, First-principles study on corrosion resistance of copper-bearing hypereutectic high chromium cast iron, *Mater. Today Commun.*, 2022, **33**, 104345.
38 S. W. Wen, Z. F. Li, C. J. Zou, W. X. Zhong, C. X. Wang, J. Chen and S. W. Zhong, Improved performances of lithium-ion batteries by conductive polymer modified copper current collector, *New J. Chem.*, 2021, **45**, 10541–10548.
39 M.-H. Lin, C.-J. Huang, P.-H. Cheng, J.-H. Cheng and C.-C. Wang, Revealing the effect of polyethylenimine on zinc metal anodes in alkaline electrolyte solution for zinc–air batteries: mechanism studies of dendrite suppression and corrosion inhibition, *J. Mater. Chem. A*, 2020, **8**, 20637–20649.
40 K. Liu, P. He, H. Bai, J. Chen, F. Dong, S. Wang, M. He and S. Yuan, Effects of dodecyltrimethylammonium bromide surfactant on both corrosion and passivation behaviors of zinc electrodes in alkaline solution, *Mater. Chem. Phys.*, 2017, **199**, 73–78.
41 J. Li, T. Zhao, E. Shangguan, Y. Li, L. Li, D. Wang, M. Wang, Z. Chang and Q. Li, Enhancing the rate and cycling performance of spherical ZnO anode material for advanced zinc-nickel secondary batteries by combined in-

situ doping and coating with carbon, *Electrochim. Acta*, 2017, **236**, 180–189.

42 Y. Dai, C. Zhang, W. Zhang, L. Cui, C. Ye, X. Hong, J. Li, R. Chen, W. Zong and X. Gao, Reversible Zn metal anodes enabled by trace amounts of underpotential deposition initiators, *Angew. Chem., Int. Ed.*, 2023, e202301192.

43 S. P. Rangarajan, Y. Barsukov and P. P. Mukherjee, In Operando Impedance Based Diagnostics of Electrode Kinetics in Li-Ion Pouch Cells, *J. Electrochem. Soc.*, 2019, **166**, A2131–A2141.

44 Y. X. Yao, X. Chen, C. Yan, X. Q. Zhang, W. L. Cai, J. Q. Huang and Q. Zhang, Regulating Interfacial Chemistry in Lithium-Ion Batteries by a Weakly Solvating Electrolyte, *Angew. Chem., Int. Ed.*, 2021, **60**, 4090–4097.

45 R. Yuksel, O. Buyukcakir, W. K. Seong and R. S. Ruoff, Metal-Organic Framework Integrated Anodes for Aqueous Zinc-Ion Batteries, *Adv. Energy Mater.*, 2020, **10**, 1904215.

46 P. Bonnick and J. Dahn, A simple coin cell design for testing rechargeable zinc-air or alkaline battery systems, *J. Electrochem. Soc.*, 2012, **159**, A981.

47 J. W. Long, K. E. Swider-Lyons, R. M. Stroud and D. R. Rolison, Design of pore and matter architectures in manganese oxide charge–storage materials, *Electrochem. Solid-State Lett.*, 2000, **3**, 453.

48 J. F. Parker, C. N. Chervin, E. S. Nelson, D. R. Rolison and J. W. Long, Wiring zinc in three dimensions re-writes battery performance—dendrite-free cycling, *Energy Environ. Sci.*, 2014, **7**, 1117–1124.

49 J. Li, Y. Cheng, M. Jia, Y. W. Tang, Y. Lin, Z. A. Zhang and Y. X. Liu, An electrochemical-thermal model based on dynamic responses for lithium iron phosphate battery, *J. Power Sources*, 2014, **255**, 130–143.

50 X. L. Xi, X. F. Li, C. H. Wang, Q. Z. Lai, Y. H. Cheng, W. Zhou, C. Ding and H. M. Zhang, Impact of Proton Concentration on Equilibrium Potential and Polarization of Vanadium Flow Batteries, *ChemPlusChem*, 2015, **80**, 382–389.

51 H. Yang, X. Meng, E. Yang, X. Wang and Z. Zhou, Effect of La addition on the electrochemical properties of secondary zinc electrodes, *J. Electrochem. Soc.*, 2004, **151**, A389.

52 M. Liu, L. Yang, H. Liu, A. Amine, Q. Zhao, Y. Song, J. Yang, K. Wang and F. Pan, Artificial solid-electrolyte interface facilitating dendrite-free zinc metal anodes via nanowetting effect, *ACS Appl. Mater. Interfaces*, 2019, **11**, 32046–32051.

53 M. Luo, C. Wang, H. Lu, Y. Lu, B. B. Xu, W. Sun, H. Pan, M. Yan and Y. Jiang, Dendrite-free zinc anode enabled by zinc-chelating chemistry, *Energy Storage Mater.*, 2021, **41**, 515–521.

54 K. E. Sun, T. K. Hoang, T. N. L. Doan, Y. Yu, X. Zhu, Y. Tian and P. Chen, Suppression of dendrite formation and corrosion on zinc anode of secondary aqueous batteries, *ACS Appl. Mater. Interfaces*, 2017, **9**, 9681–9687.

55 M. Deyab, Hydroxyethyl cellulose as efficient organic inhibitor of zinc–carbon battery corrosion in ammonium chloride solution: Electrochemical and surface morphology studies, *J. Power Sources*, 2015, **280**, 190–194.